# Modeling of a Thick Cylindrical Pneumatic Leg for a Soft Parallel Robot

Zeinab Awada, Hamza El Jjouaui, Marc Gouttefarde, Yassine Haddab

# Modeling of a Thick Cylindrical Pneumatic Leg for a Soft Parallel Robot

Zeinab Awada[1], Hamza El Jjouaoui[1], Marc Gouttefarde[1], Yassine Haddab[1]

*Abstract*— **Soft manipulators have experienced a significant development over the past few years thanks to their versatility, compliance, and safety. Soft manipulators made of hyperelastic materials present a modeling challenge due to their combined geometric and material nonlinearity, alongside their leveraged compliance. This paper considers a thick cylindrical pneumatic actuator in the context of a soft parallel robot. The input pressure and the external axial force to which it is subjected are modeled. The analytical solutions for these models are then derived using the Yeoh strain energy density function. The advantage of using the Yeoh material model is guaranteeing the existence of an analytical solution regardless of the material used for the fabrication of the cylindrical actuator. The accuracy of the models is evaluated using Finite Element Analysis, and a sensitivity analysis is also carried out to test their robustness. Finally, experimental results are provided and the importance of the material characterization is highlighted. The purpose of this work is to lay the foundation for future studies in modeling a soft parallel robot with three soft thick cylindrical "legs".**

## I. Introduction

With the increasing demand for safe and lightweight manipulators, soft robotics have recently witnessed a remarkable progress in various fields. For example, soft manipulators are particularly promising in agriculture. For harvesting fragile crops, soft grippers have been proposed [1]. Soft grippers have also been used in underwater tasks, and bio-inspired soft robotics have empowered ocean exploration and underwater operations [2]. From the depths of the ocean to the human body, soft manipulators have also been developed for medical applications such as minimally invasive surgery [3].

The above mentioned applications share common design specifications: Safety, compliance, and adaptability. Soft robots meet these requirements thanks to their design structure, material composition, or both. For example, among other material choices, some soft robots meet the above design requirements by using hyperelastic or Green elastic material. This leverages the compliance of the structure thanks to the inherent microstructural-level adaptability of the material used. Indeed, the nonlinear stress-strain relation of hyperelastic materials allows them to exhibit strains as high as 1000%. However, the nonlinearity of these materials makes their modeling a challenging task. The lack of analytical models notably complicates the design of soft manipulators and leads to non-intuitive design choices.

Starting from here, this paper presents the modeling of a thick cylindrical hyperelastic pneumatic actuator. This actuator serves as a soft link for a 5 degree-of-freedom soft parallel robot (SPR) shown in Fig. 1 and is therefore modelled under the corresponding working conditions. Asides to the internal pressure, each pneumatic actuator might be subjected to an external pressure at its lateral sides, especially during underwater operations. A preliminary study with simplifying assumptions is considered where the weight of the platform of the SPR along with external loads are only considered as an external axial force acting on the three thick cylindrical pneumatic actuators. Thick cylindrical actuators are chosen over thin ones due to their ease of fabrication. Simultaneously, the mathematical modeling of thick actuators is more complex than that of thin actuators.

In [4], a thick cylindrical actuator is studied. The internal pressure and the external axial force are expressed as a function of complex integrals of the strain energy density function (or material model) of the hyperelastic material used. It is later pointed out in [5] that there are almost no analytical solutions for the stress analysis of such a structure mostly due to the mathematical complexity of material models. Therefore, in [4] and [5], a stability analysis is carried out on a thick cylindrical actuator using four material models: Neo-Hookean, Varga, Mooney-Rivlin, and Ogden. The first two are mathematically simple, but they are only accurate for small strains [6, p. 242]. The Mooney-Rivlin model is compatible with small to medium strains and is too simple to characterize certain hyperelastic materials [6, p. 243]. The Ogden model, renowned for its accuracy even at high strains, incorporates exponential material constants. Although the authors in [4], [5] have considered mathematically simple material constants, this assumption does not extend to hyperelastic materials commonly used in soft robotics. Extensive literature reviews indicate that within the domain of soft manipulators utilizing hyperelastic materials, the exponential material constants of the Ogden model take irrational values [7]–[9]. These irrational values lead to very complex or non-existent analytical solutions for the pressure and axial force models as demonstrated in Section III. Therefore, the first contribution of this paper is to propose analytical solutions for the pressure and the axial force models regardless of the hyperelastic material used. These models are derived in Section III from the Yeoh material model which is accurate for large deformations [10] and is one of the most common strain energy density functions to characterize hyperelastic materials used in soft robotics [7]–[9]. The pressure and axial force models are expressed as a function of the axial and radial deformations of the thick cylindrical actuator. Their detailed derivation and proof is provided in Section II.

[1]LIRMM, Univ Montpellier, CNRS, Montpellier, France.

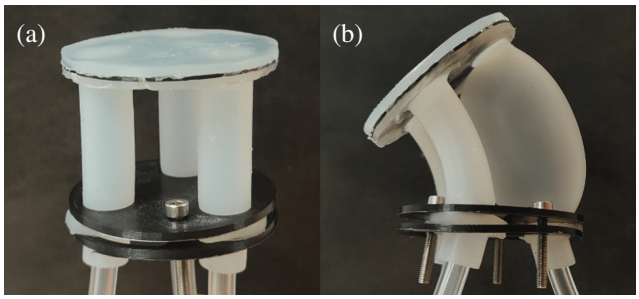


Fig. 1. A soft parallel robot with 3 soft thick cylindrical pneumatic actuators serving as links between the platform and the base in (a) rest configuration and in (b) actuated configuration .

Several works have studied the bifurcation of thick cylindrical actuators [4], [5], [11]–[13] by plotting the pressure model for a fixed axial deformation or a fixed axial force. Moreover, the axial force is always calculated for a constant axial deformation. First, this does not correspond to the work conditions of an SPR where the axial deformation is either unconstrained or dependent on the variable applied axial force. Second, none of these works assess the accuracy and robustness of the pressure and axial force models. Therefore, the second contribution of this paper is to evaluate the accuracy of these models using FEA and experimental results and to assess their robustness by carrying out a sensitivity analysis towards the deformations and the material constants of the cylindrical actuator.

This paper is organized as follows: Section II presents the models of the pressure and axial force of the cylindrical actuator. In Section III, the analytical solutions to the previous models are obtained using Yeoh strain energy density function which is compared to the Ogden material model. The experimental setup used to validate the proposed models along with the simulation and experimental results models are presented in Section IV. The work is finally concluded in Section V.

## II. Modeling of a Thick Cylindrical Hyperelastic Pneumatic Actuator

In this section, a thick cylindrical hyperelastic actuator of an SPR is modeled where the differential pressure and the applied axial force are expressed as a function of the radial and axial deformations of the actuator. The cylinder is closed at both ends with only the lower end fixed. It is characterized by an initially undeformed length $L$ (cavity length $l$), internal radius $R_{in}$, and external radius $R_{ex}$ as shown in Fig. 2(a). It is actuated by an internal pressure, $p_{in}$, and subjected to an external pressure, $p_{ex}$, acting on its lateral walls. The external pressure, $p_{ex}$, mirrors interactions with the surrounding as when working underwater or in a compact environment that exerts a lateral load on the external walls of the actuator. Moreover, a simplifying assumption is made where external loads are represented by an axial force, $f_{ex}$. To model the actuator, a cylindrical coordinate basis, $\{e_r, e_\theta, e_z\}$, is associated to the reference undeformed

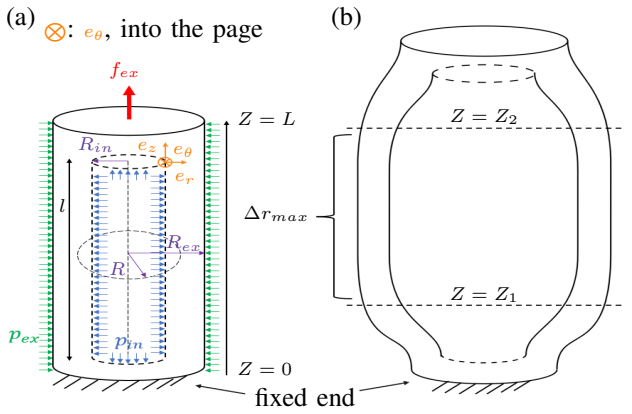


Fig. 2. (a) Initially undeformed thick cylinder, fixed at its lower end and subjected to internal pressure $p_{in}$, external pressure $p_{ex}$, and external axial force $f_{ex}$. (b) Thick cylinder radially and axially deformed under the effect of $p_{in}$, $p_{ex}$, and $f_{ex}$.

configuration where each material point is described by a set of 3 coordinates $(R, \Theta, Z)$. In what follows, uppercase variables $(R, \Theta, Z)$, will be used to refer to material points in the undeformed configuration and lowercase ones $(r, \theta, z)$ to material points in the deformed configuration.

When subjected to an internal pressure $p_{in}$, external pressure $p_{ex}$, and external axial force $f_{ex}$, the actuator deforms radially and axially. As shown in Fig. 2(b), the radial deformation is non-uniform along $e_z$. It is zero at $Z = 0$ because the lower base of the cylinder is fixed and then gradually increases to reach a maximum, $\Delta r_{max}$, at $Z = Z_1$. It may then remain constant over a considerable portion of the cylinder, $Z_1 \leq Z \leq Z_2$. However, since the considered cylinder is closed at both ends, the radial deformation decreases between $Z_2 \leq Z \leq L$. Therefore, the radial coordinate after deformation reads

$$r = f_1(R, Z), \ \frac{\partial f_1}{\partial Z} = 0 \ \forall Z \in [Z_1, Z_2] \tag{1}$$

The axial deformation is considered constant in the radial direction. This is because the cross-section of the actuator is considered to remain planar due to the absence of axial shear. It is further assumed that, for $Z \geq Z_1$, the axial deformation is homogeneous along the axial direction. Therefore, the axial coordinate after deformation reads

$$z = f_2(Z), \ f_2(Z) = \lambda_z Z \ \forall Z \in [Z_1, Z_2] \tag{2}$$

Finally, in the absence of torsional effects, the azimuth is constant, i.e.

$$\theta = \Theta \tag{3}$$

Therefore, in cylindrical basis, the deformation matrix $\mathbf{F}$ reads

$$\mathbf{F} = \begin{bmatrix} \frac{\partial r}{\partial R} & \frac{\partial r}{R\partial\Theta} & \frac{\partial r}{\partial Z} \\ \frac{r\partial\theta}{\partial R} & \frac{r\partial\theta}{R\partial\Theta} & \frac{r\partial\theta}{\partial Z} \\ \frac{\partial z}{\partial R} & \frac{\partial z}{R\partial\Theta} & \frac{\partial z}{\partial Z} \end{bmatrix} = \begin{bmatrix} \frac{\partial f_1}{\partial R} & 0 & \frac{\partial f_1}{\partial Z} \\ 0 & \frac{r}{R} & 0 \\ 0 & 0 & \frac{\partial f_2}{\partial Z} \end{bmatrix} \tag{4}$$

Since the region $Z_1 \leq Z \leq Z_2$ dominates the deformation of the cylinder, especially at large deformations, attention can

be limited to this region and hence $\frac{\partial f_2}{\partial Z} = \lambda_z$ and $\mathbf{F}$ becomes a diagonal matrix (since $\frac{\partial f_1}{\partial Z} = 0$). The diagonal terms are called the principal stretches and read

$$\lambda_r = \frac{\partial f_1}{\partial R},\ \lambda_\theta = \frac{r}{R},\ \lambda_z = \frac{z}{Z} \tag{5}$$

In addition, the Cauchy stress tensor, $\boldsymbol{\sigma}$, over $Z_1 \leq Z \leq Z_2$ is

$$\boldsymbol{\sigma} = \begin{bmatrix} \sigma_r & 0 & 0 \\ 0 & \sigma_\theta & 0 \\ 0 & 0 & \sigma_z \end{bmatrix} \tag{6}$$

where $\sigma_r, \sigma_\theta$, and $\sigma_z$ are the radial, hoop, and axial stresses, respectively. Knowing that $p_{in}$ and $p_{ex}$ act on the internal and external lateral faces of the cylinder, respectively, a boundary condition on $\sigma_r$ is derived as

$$\begin{aligned} \sigma_r &= -p_{in} \text{ at } r = r_{in} \\ \sigma_r &= -p_{ex} \text{ at } r = r_{ex} \end{aligned} \tag{7}$$

Moreover, an isochoric deformation, i.e. incompressible material, is considered, which implies a conservation of volume throughout deformation [6, p. 222]. For example, the volume comprised between $R_{in}$ and $R$ and the axial coordinates 0 and $Z$ is conserved after deformation, hence

$$z(r^2 - r_{in}^2) = Z(R^2 - R_{in}^2) \tag{8}$$

The ratio between the undeformed volume, $V_0$, and the current deformed volume, $V$, is equal to the determinant of the deformation matrix $\mathbf{F}$ as demonstrated in [6, p. 74]. Therefore, the conservation of volume can be alternatively expressed as

$$\lambda_r \lambda_\theta \lambda_z = 1 \tag{9}$$

Applying Cauchy's first law of motion, the divergence of the stress tensor is zero $\boldsymbol{\nabla} \cdot \boldsymbol{\sigma} = 0$, [6, pp. 141-145], hence

$$r\frac{d\sigma_r}{dr} + \sigma_r - \sigma_\theta = 0 \tag{10}$$

For an incompressible isotropic hyperelastic material with strain energy density function $W(\lambda_r, \lambda_\theta, \lambda_z)$, the principal stresses read [6, pp. 222-225]

$$\sigma_i = -p_{in} + \lambda_i \frac{\partial W}{\partial \lambda_i}\ \forall i = r, \theta, z \tag{11}$$

Using Eq. (9) and introducing the notation $\hat{W}(\lambda_\theta, \lambda_z) = W((\lambda_\theta \lambda_z)^{-1}, \lambda_\theta, \lambda_z)$, the partial derivatives of $W$ are expressed as functions of the partial derivatives of $\hat{W}$ as follows

$$\begin{aligned} \frac{\partial \hat{W}}{\partial \lambda_\theta} &= \frac{\partial W}{\partial \lambda_r}\frac{\partial \lambda_r}{\partial \lambda_\theta} + \frac{\partial W}{\partial \lambda_\theta}\frac{\partial \lambda_\theta}{\partial \lambda_\theta} + \frac{\partial W}{\partial \lambda_z}\frac{\partial \lambda_z}{\partial \lambda_\theta} \\ \frac{\partial \hat{W}}{\partial \lambda_\theta} &= -{\lambda_z}^{-1}{\lambda_\theta}^{-2}\frac{\partial W}{\partial \lambda_r} + \frac{\partial W}{\partial \lambda_\theta} \\ \lambda_r \frac{\partial W}{\partial \lambda_r} &= \lambda_\theta \frac{\partial W}{\partial \lambda_\theta} - \lambda_\theta \frac{\partial \hat{W}}{\partial \lambda_\theta} \end{aligned} \tag{12}$$

Using Eq. (12), $\sigma_r - \sigma_\theta$ and $\sigma_r - \sigma_z$ are evaluated

$$\sigma_r - \sigma_\theta = -\lambda_\theta \frac{\partial \hat{W}}{\partial \lambda_\theta} \tag{13}$$

$$\sigma_r - \sigma_z = -\lambda_z \frac{\partial \hat{W}}{\partial \lambda_z} \tag{14}$$

To express $p_{in}$ in terms of $\lambda_\theta, \lambda_z$, and $p_{ex}$, Eq. (8) is used to derive $\frac{dr}{r}$ as a function of $\lambda_\theta$ and $\lambda_z$. Thus, the following relation holds

$$\begin{aligned} R &= \left(\lambda_z(r^2 - r_{in}^2) + R_{in}^2\right)^{\frac{1}{2}} \\ \frac{R}{r} &= \left(\frac{\lambda_z(r^2 - r_{in}^2) + R_{in}^2}{r^2}\right)^{\frac{1}{2}} \\ \lambda_\theta &= \left(\frac{r^2}{\lambda_z(r^2 - r_{in}^2) + R_{in}^2}\right)^{\frac{1}{2}} \end{aligned} \tag{15}$$

Finally, the following relation between $d\lambda_\theta$ and $dr$ is derived from Eq. (15)

$$r\frac{d\lambda_\theta}{dr} = \lambda_\theta - \lambda_z {\lambda_\theta}^3 \tag{16}$$

Using Eq. (7), denoting $\Delta p = p_{in} - p_{ex}$, and substituting Eq. (13) and Eq. (16) in Eq. (10), the relation between $\Delta p$, $\lambda_\theta$, and $\lambda_z$ is obtained

$$\begin{aligned} r\frac{d\sigma_r}{dr} + \sigma_r - \sigma_\theta &= 0 \\ d\sigma_r &= \frac{dr(\sigma_\theta - \sigma_r)}{r} \\ \Delta p &= \int_{r_{in}}^{r_{ex}} \frac{\lambda_\theta}{r}\frac{\partial \hat{W}}{\partial \lambda_\theta} dr \\ \Delta p &= \int_{\lambda_{ex}}^{\lambda_{in}} ({\lambda_\theta}^2 \lambda_z - 1)^{-1} \frac{\partial \hat{W}}{\partial \lambda_\theta} d\lambda_\theta \end{aligned} \tag{17}$$

where $\lambda_{in} = \frac{r_{in}}{R_{in}}$ and $\lambda_{ex} = \frac{r_{ex}}{R_{ex}}$.
As shown in Fig. 3, the force equilibrium in the axial direction reads

$$f_{iz} = p_{in}\pi r_{in}^2 + f_{ex} \tag{18}$$

where $f_{iz}$ is the internal force generated at the cross-section of the cylinder and is defined by $f_{iz} = 2\pi \int_{r_{in}}^{r_{ex}} \sigma_z r dr$. Along with Eq. (18), the expression of $f_{iz}$ can be used to derive that of $f_{ex}$. Using Eq. (16), $f_{iz}$ is expressed in terms of $\lambda_\theta$ and $\lambda_z$ as follows

$$\begin{aligned} f_{iz} &= 2\pi \int_{\lambda_{in}}^{\lambda_{ex}} \sigma_z \frac{r^2}{\lambda_\theta - \lambda_z {\lambda_\theta}^3} d\lambda_\theta \\ &= 2\pi \int_{\lambda_{ex}}^{\lambda_{in}} \sigma_z \frac{\lambda_\theta r^2}{\lambda_\theta^2(\lambda_z \lambda_\theta^2 - 1)} d\lambda_\theta \end{aligned} \tag{19}$$

From the conservation of volume Eq. (8), the following property is deduced

$$R^2(\lambda_\theta^2 \lambda_z - 1) = R_{in}^2(\lambda_{in}^2 \lambda_z - 1) = R_{ex}^2(\lambda_{ex}^2 \lambda_z - 1) \tag{20}$$

Substituting $\frac{r^2}{\lambda_\theta^2} = R^2$ in Eq. (19), and using the property in Eq.(20), $f_{iz}$ is obtained

$$f_{iz} = \pi R_{in}^2(\lambda_{in}^2 \lambda_z - 1) \int_{\lambda_{ex}}^{\lambda_{in}} \frac{2\sigma_z \lambda_\theta}{(\lambda_z \lambda_\theta^2 - 1)^2} d\lambda_\theta \tag{21}$$

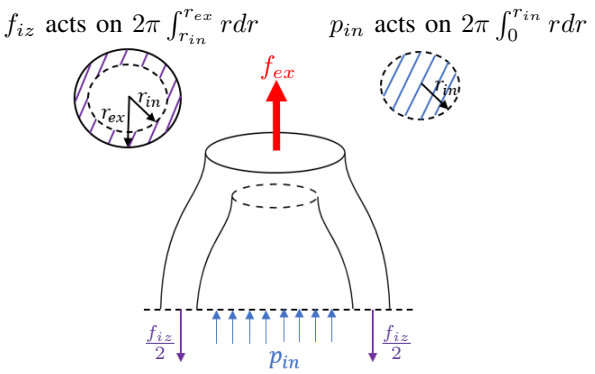


Fig. 3. Section of a closed cylinder with external axial force $f_{ex}$ acting on its upper surface, actuated by $p_{in}$, and having an induced internal axial force $f_{iz}$.

Using Eq. (14) and Eq. (10), $\sigma_z$ is expressed as follows

$$\sigma_z = -p_{ex} + \lambda_z \frac{\partial \hat{W}}{\partial \lambda_z} - \int_{\lambda_{ex}}^{\lambda_\theta} \frac{\frac{\partial \hat{W}}{\partial \lambda_\theta}}{(\lambda_z \lambda_\theta^2 - 1)} d\lambda_\theta \tag{22}$$

Substituting $\sigma_z$ in Eq. (21) leads to

$$\frac{f_{iz}}{\pi R_{in}^2 (\lambda_{in}^2 \lambda_z - 1)} = \int_{\lambda_{ex}}^{\lambda_{in}} \frac{2\lambda_z \frac{\partial \hat{W}}{\partial \lambda_z} \lambda_\theta}{(\lambda_z \lambda_\theta^2 - 1)^2} d\lambda - \int_{\lambda_{ex}}^{\lambda_{in}} \frac{2 p_{ex} \lambda_\theta}{(\lambda_z \lambda_\theta^2 - 1)^2} d\lambda_\theta - \int_{\lambda_{ex}}^{\lambda_{in}} \frac{2\lambda_\theta}{(\lambda_z \lambda_\theta^2 - 1)^2} \left( \int_{\lambda_{ex}}^{\lambda_\theta} \frac{\frac{\partial \hat{W}}{\partial \lambda_\theta}}{(\lambda_z \lambda_\theta^2 - 1)} d\lambda_\theta \right) d\lambda_\theta \tag{23}$$

Using integration by parts to evaluate the last term of the above integral, $\int u'v = uv - \int uv'$, where $u = \frac{\lambda_\theta^2}{(\lambda_z \lambda_\theta^2 - 1)}$ and $v = \int_{\lambda_{ex}}^{\lambda_\theta} \frac{\frac{\partial \hat{W}}{\partial \lambda_\theta}}{(\lambda_z \lambda_\theta^2 - 1)} d\lambda_\theta$, the expression of $f_{iz}$ is

$$\frac{f_{iz}}{\pi R_{in}^2} = (\lambda_{in}^2 \lambda_z - 1) \int_{\lambda_{ex}}^{\lambda_{in}} \frac{2\lambda_z \frac{\partial \hat{W}}{\partial \lambda_z} - \lambda_\theta \frac{\partial \hat{W}}{\partial \lambda_\theta}}{(\lambda_z \lambda^2 - 1)^2} \lambda_\theta d\lambda_\theta + p_{in} \lambda_{in}^2 - p_{ex} \lambda_{ex}^2 \frac{R_{ex}^2}{R_{in}^2} \tag{24}$$

Referring to Eq. (18), the expression of the external axial $f_{ex}$ is given by

$$f_{ex} = \pi R_{in}^2 (\lambda_{in}^2 \lambda_z - 1) \int_{\lambda_{ex}}^{\lambda_{in}} \frac{2\lambda_z \frac{\partial \hat{W}}{\partial \lambda_z} - \lambda_\theta \frac{\partial \hat{W}}{\partial \lambda_\theta}}{(\lambda_z \lambda_\theta^2 - 1)^2} \lambda_\theta d\lambda_\theta - p_{ex} \pi \lambda_{ex}^2 R_{ex}^2 \tag{25}$$

Eq. (25) shows that an increase in the axial deformation and its corresponding impact on the strain energy density function contributes to the axial force and vice versa for the radial deformation.

## III. Analytical Solutions using Yeoh Strain Energy Density Function

The pressure and axial force models in Eq. (17) and Eq. (25) respectively, are expressed as a function of an integral of the strain energy density function. According to [4], [5], the Ogden material model is the most accurate in representing stability compared to the Neo-Hookean, Varga, and Mooney-Rivlin models. In terms of the principal stretches, $\lambda_r, \lambda_\theta$, and $\lambda_z$, the Ogden model reads

$$W = \sum_{i=1}^{N} \frac{\mu_i}{\alpha_i} \left( \lambda_r^{\alpha_i} + \lambda_\theta^{\alpha_i} + \lambda_z^{\alpha_i} - 3 \right) \tag{26}$$

where $N$ is the polynomial order and $\mu_i$ and $\alpha_i$ are material constants. As shown in [7]–[9], the exponential material constants of the Ogden models of the hyperelastic materials frequently used in soft robotics are irrational numbers. This leads to the non-integrability of Eq. (17) and Eq. (25). For example, the Ogden model of Ecoflex™ 0050- Smooth-on Inc. is $\mu_1 = 0.7363, \alpha_1 = 2.858, \mu_2 = 0.8074, \alpha_2 = 2.604, \mu_3 = -1.526$, and $\alpha_3 = 2.740$ [8]. In this case, the software Maple gives a complex analytical solution for the pressure model with more than 800 terms. As for the axial force, Maple issues an error indicating the excessive length of the analytical solution. Primarily, the complexity of the expressions is due to the irrational exponential material constants, $\alpha_i$, present in the Ogden model. We therefore adopt the Yeoh model which is abundantly used to characterize hyperelastic materials [7]–[9] and is known to be accurate especially for large deformations of rubber [10].

The strain energy density function reads [14]

$$W = \sum_{i=1}^{N} C_i \left( \lambda_r^2 + \lambda_\theta^2 + \lambda_z^2 - 3 \right)^i \tag{27}$$

where $N$ is the polynomial order and $C_i$ are the material constants. For a third-order Yeoh model ($i$ = 3), the pressure and axial force analytical solutions are computed using Maple software as a function of $C_1$, $C_2$, and $C_3$. They read respectively

$$\Delta p = \tilde{p}(\lambda_{in}, \lambda_z) - \tilde{p}(\lambda_{ex}, \lambda_z) \tag{28}$$

$$f_{ex} = \tilde{f}(\lambda_{in}, \lambda_z) - \tilde{f}(\lambda_{ex}, \lambda_z) \tag{29}$$

where the expressions of $\tilde{p}(\lambda_\theta, \lambda_z)$ and $\tilde{f}(\lambda_\theta, \lambda_z)$ are given in [15].

## IV. Experimental Setup and Results

### A. Materials and experimental setup

For the FEA simulations and the experiments, Ecoflex™ 0050- Smooth-on Inc. is used. Several Yeoh models exist to describe its strain energy density function [8], [16]–[19]. As shown in Fig. 4, the uniaxial stress-strain curves of the five models are distinct. The variation of the material behavior depends on its storing conditions, mixing composition, and fabrication process. For the FEA simulation, the first model (blue curve) is used and is referred to as the reference model hereafter: $C_{1r}$ = 15.8, $C_{2r}$ = -0.48, and $C_{3r}$ = 0.113 kPa. To evaluate the performance and the accuracy of the model, the deformations of the cylindrical pneumatic actuators are measured when it is pressurized (cf. Fig. 5). A laser sensor (Keyence LK-H152, range = 80 mm, resolution = 0.25 $\mu$m) measures the axial deformation at the top end and another laser sensor (Acuity AR100, range = 50 mm, resolution = 5 $\mu$m) measures the radial deformation at the middle of the

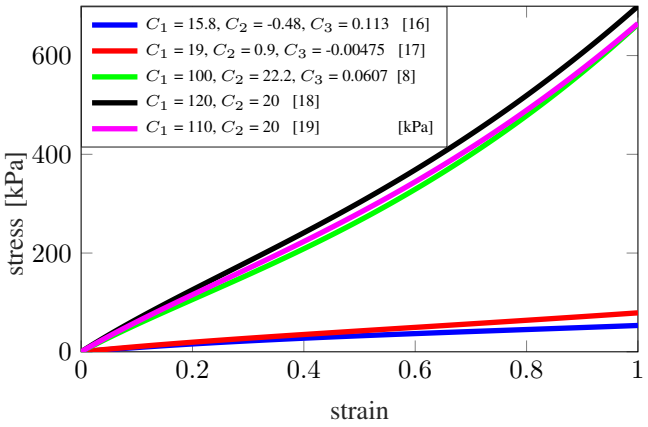


Fig. 4. Stress-strain curves of Ecoflex-0050 for uniaxial tests fitted to 2nd and 3rd order Yeoh models gathered from literature.

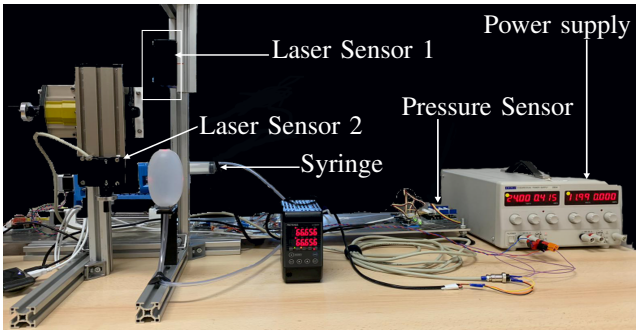


Fig. 5. Experimental set-up used to characterize a cylindrical pneumatic actuator.

cylinder. Moreover, an axial force is applied and measured using a force sensor (Sauter, resolution = 0.02 N).

### *B. FEA simulation results*

A thick cylinder of internal radius $R_{in} = 4$ mm, external radius $R_{ex} = 6$ mm, and cavity length $l = 30$ mm is considered. Using ANSYS and following [20], the cylinder is simulated using Static Structural Analysis. The following settings are used: The actuator is meshed by 1 mm tetrahedral elements of quadratic order and nonlinear mechanics preference. Large deflections and auto-time stepping are enabled with 10 ms minimum time step and 50 ms maximum time step. The results of two simulations are presented in this section: First, the actuation pressure is increased from 0 kPa to 45 kPa over 100 steps and in the absence of an external force. Then, for the same actuation pressure, a ramp external force $f_{ex}$ of slope $f_{max}$ = 0.35 N/step is applied.

*1) Accuracy:* As shown in Fig. 6(a)-(b), in the absence of $f_{ex}$, the pressure model presented in Eq. (17) aligns with the FEA results with a maximum error of 7.3%. However, in the presence of $f_{ex}$ two phases are identified: (1) The first is defined at the state of deformation ($\lambda_{ex} < \lambda^*_{ex}$, $\lambda_z < \lambda^*_z$) or $\Delta p <$ 6.4 kPa where the model tends to underestimate the pressure. (2) The second is defined at ($\lambda_{ex} \geq \lambda^*_{ex}, \lambda_z \geq \lambda^*_z$) or $\Delta p \geq$ 6.4 kPa where the model converges back to the FEA results. In the first phase, the tensile force dominates the deformation of the actuator. Therefore, for the same actuation pressure, the axial stretch increases more than the radial stretch. Hence, the model in Eq. (17) tends to underestimate the required actuation pressure to reach this state of deformation. Multiple simulations are conducted with progressively higher values of $f_{max}$, revealing a corresponding increase in the value of the pair $(\lambda^*_{ex}, \lambda^*_z)$, thereby supporting the earlier explanation. For $\Delta p >$ 6.4 kPa, the actuation pressure becomes more dominant than $f_{ex}$ and the error between the pressure model and the FEA results decreases to 6.4%.

Even though it predominantly governs the actuator deformation, the force model described in Eq. (25) underestimates $f_{ex}$ for ($\lambda_{ex} < \lambda^*_{ex}$, $\lambda_z < \lambda^*_z$) as shown in Fig. 6(d)-(e). This discrepancy can be elucidated by closely examining the force model, which comprises two dominant terms: One as an integral of $+\lambda_z \frac{\partial \hat{W}}{d\lambda_z}$ and the other as an integral of $-\lambda_z \frac{\partial \hat{W}}{d\lambda_z}$. In essence, axial deformation and its impact on the strain energy function increase the mathematical value of the axial force, while an increase in radial stretch decreases it. However, upon examining the values of the integrals calculated by these two components, it becomes apparent that the second term contributes more significantly to the value of $f_{ex}$. Consequently, even though the axial force surpasses the pressure, the positive value produced by the first integral fails to compensate for that produced by the second one. For ($\lambda_{ex} \geq \lambda^*_{ex}, \lambda_z \geq \lambda^*_z$), the pressure becomes more dominant and hence the second integral term becomes positive and the force model converges towards the FEA results but with an increasing error that reaches a maximum of 10.6% at $\Delta p$ = 45 kPa and $f_{ex} = 35$ N.

Therefore, the FEA suggest that in the absence of $f_{ex}$ the model presented in Eq. (17) is accurate with a maximum error of 6.4%. In the presence of an axial force and beyond the deformation state $(\lambda^*_{ex}, \lambda^*_z)$, the pressure and force models are accurate up to an error of 6.4% and 10.4% respectively. Before this state of deformation, the models underestimate the values of $\Delta p$ and $f_{ex}$. This calls for integrating a coupling factor in Eq. (17) and Eq. (25) to represent the influence of the axial force and the pressure on each other.

*2) Robustness and sensitivity analysis:* The robustness of the two models, Eq. (17) and Eq. (25), to the axial stretch $\lambda_z$, and the radial stretch at the external wall $\lambda_{ex}$, is evaluated in Fig. 6(c)-(f). To measure the impact of $\lambda_{ex}$ on $\Delta p$, $\lambda_z$ is held constant while $\lambda_{ex}$ is varied and vice versa.

Fig. 6(c) suggests that $\lambda_{ex}$ has a more significant impact on the pressure model than $\lambda_z$. The sensitivity of the pressure model to variations in $\lambda_{ex}$ is described by the relationship $\frac{\partial \Delta p}{\partial \lambda_{ex}} = \alpha e^{\beta \lambda_{ex}}$ , where $\alpha > 0$ and $\beta > 0$, derived through data fitting. On the contrary, as indicated by Fig. 6(e), the force model is more responsive to variations in the axial stretch $\lambda_z$. This sensitivity is described by a second degree polynomial $\frac{\partial f_{ex}}{\partial \lambda_z} = \alpha \lambda_z^2 + \beta \lambda_z + \gamma$, where $\alpha > 0$ and $\gamma > 0$, derived through data fitting. Moreover, $f_{ex}$ exhibits little variation when $\lambda_{ex} \leq 2$, suggesting a minor impact of $\lambda_{ex}$ on $f_{ex}$. However, as $\lambda_{ex}$ surpasses 2, its influence on $f_{ex}$

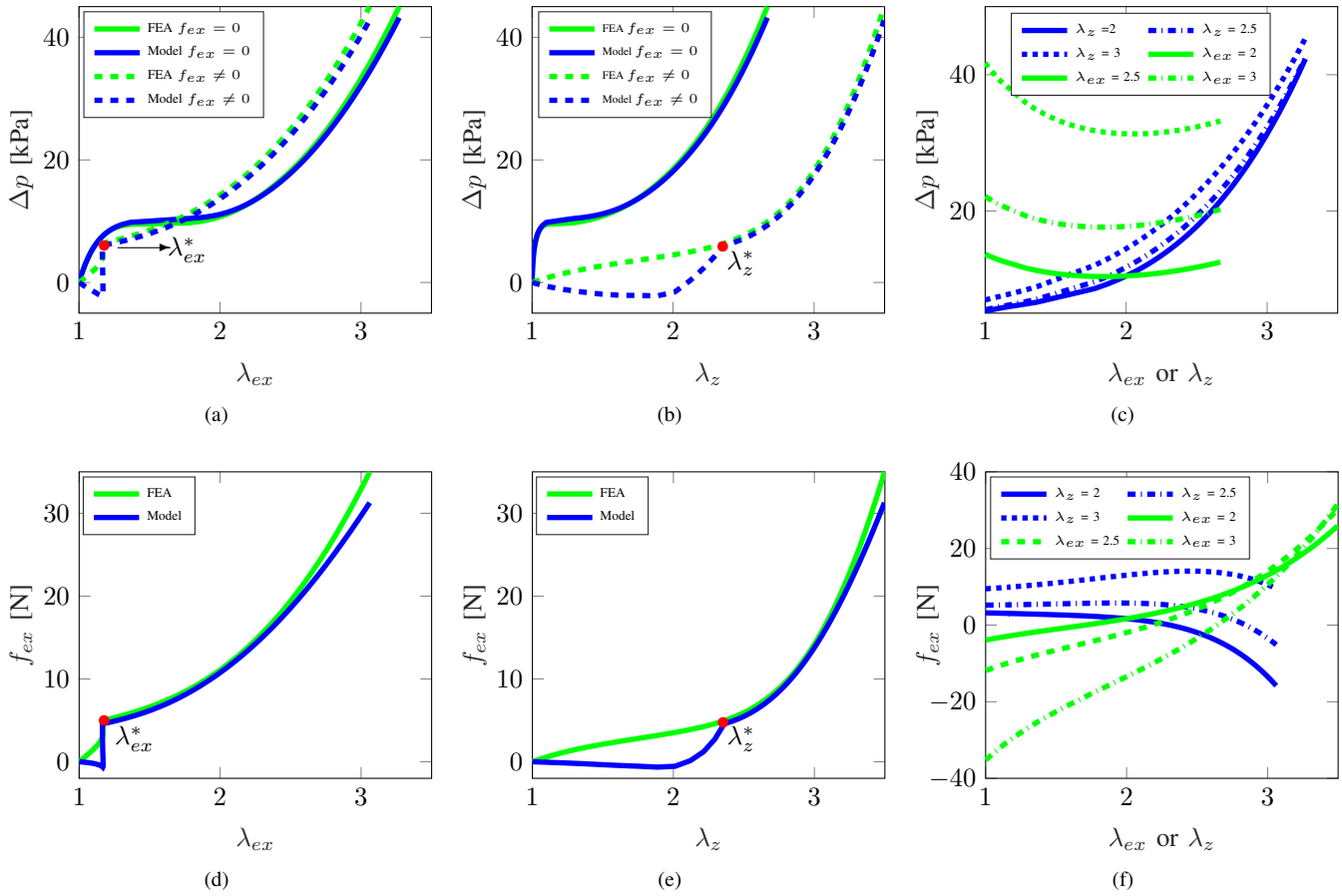


Fig. 6. FEA-based validation of (a)-(b) the pressure and (d)-(e) the external axial force models plotted as a function of (a)-(d) the radial stretch at the external wall $\lambda_{ex}$ and (b)-(c) the axial stretch $\lambda_z$. The pressure model is evaluated in (a)-(b) in the absence (solid line) and presence (dotted line) of an external axial force $f_{ex}$. (c)-(f) Pressure and force model sensitivity to $\lambda_{ex}$(blue) and $\lambda_z$ (green).

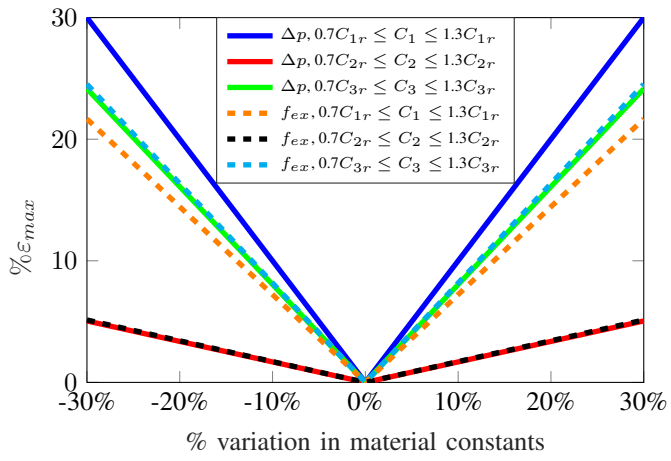


Fig. 7. Maximum variations $\varepsilon_{max}$ for $\Delta p$ and $f_{ex}$ when the three Yeoh material constants $C_1$, $C_2$, and $C_3$ are altered by $\pm$ 30% with respect to the reference values: $C_{1r}$ = 15.8, $C_{2r}$ = 0.48, and $C_{3r}$ = 0.113 kPa. $\varepsilon_{max}$ is calculated with respect to a reference $\Delta p$ and $f_{ex}$ corresponding to the reference values $C_{1r}$, $C_{2r}$, and $C_{3r}$.

becomes more pronounced. Therefore, the robustness of the pressure model drastically decreases with high variations of the radial stretch whereas the robustness of the force model is subject to variations of the axial stretch.

Moreover, as reported in our work [15], the Yeoh material constants, $C_1$, $C_2$, and $C_3$, dominate the pressure and force models. According to the literature reviews and Fig. 4, the two material models of Ecoflex™ 0050 having the closest stress-strain behavior have a percentage difference of: 20%, 280%, and 100% on $C_1$, $C_2$, and $C_3$ respectively. The inconsistency in the material characterization calls for studying the effect of the three material constants on the pressure and force models. Therefore, in an optimistic outlook, the three material constants are only varied by $\pm$ 30% with respect to the reference model: $C_{1r} = 15.8$, $C_{2r} = -0.48$, $C_{3r}$ = 0.113 kPa. The corresponding detailed variations of the pressure and force models are reported in [15] but for the sake of brevity, only the maximum variations of the models are reported in Fig. 7. The following points are concluded from this study: (1) The maximum variations of the pressure and force models $\varepsilon_{max}$ exhibits a linear relation with the variations of $C_1$, $C_2$, and $C_3$. This relation is symmetric with respect to the y-axis. For example, a -10% decrease and a +10% increase in any of the material constants yields the same $\varepsilon_{max}$. (2) The pressure model $\Delta p$ is the most sensitive to variations in $C_1$. A 30% increase in $C_1$ leads to a 30%

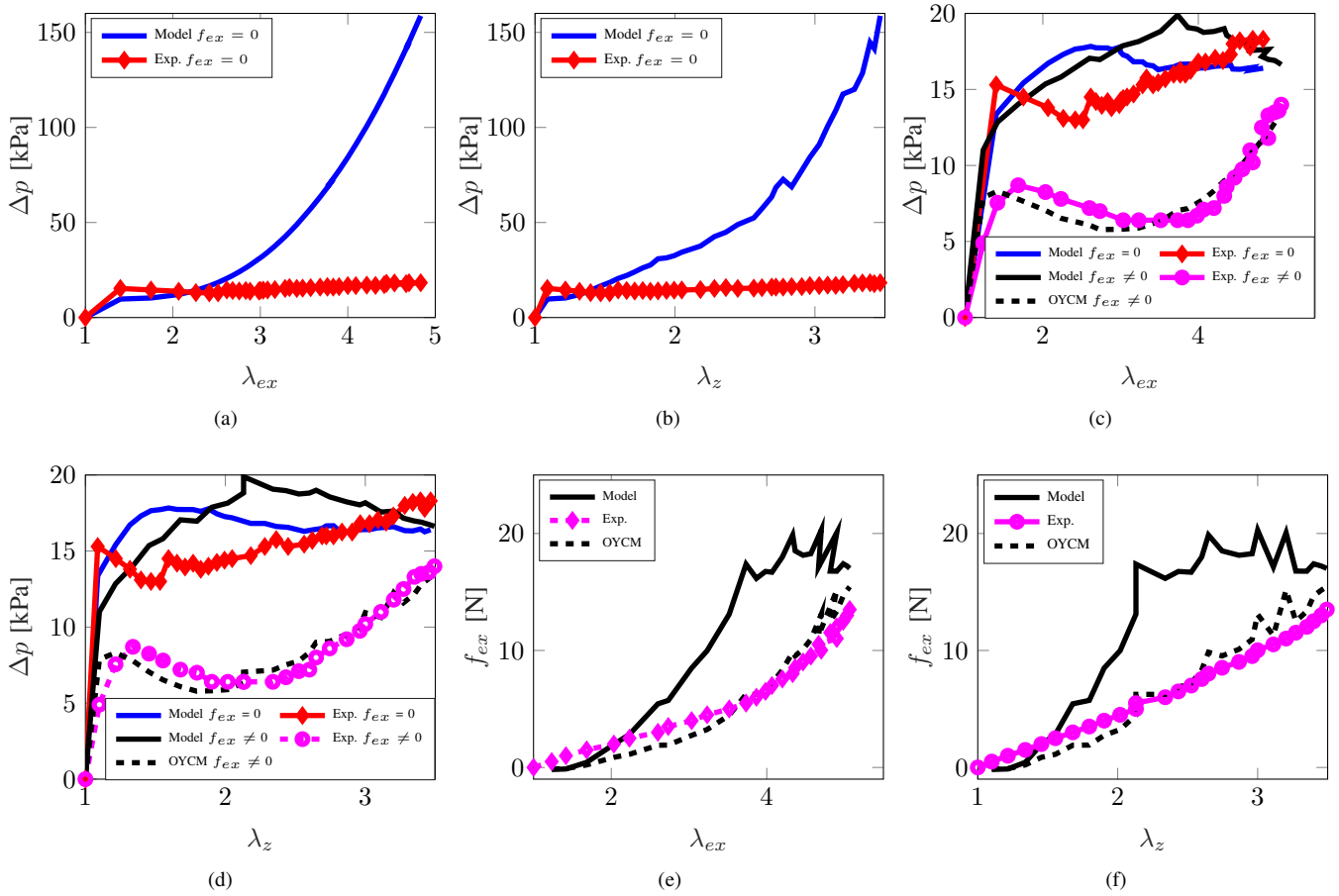


Fig. 8. (a)-(b) Experimental results (red curve) and pressure model computed using the reference material model (blue curve) for a pressurized cylindrical actuator in the absence of an axial force. (c)-(d) Experimental results (red in the absence of $f_{ex}$ and magenta in the presence of $f_{ex}$) along with the pressure model when a new Yeoh model is considered $C_1 = 19$, $C_2 = 0.9$, and $C_3$ = -0.00475 kPa (blue curve in the absence of $f_{ex}$ and solid black curve in the presence of $f_{ex}$). The pressure model in the presence of an axial force is re-evaluated using Yeoh constants computed using an optimization algorithm, referred to as OYCM in the legend (dotted black line). (e)-(f) Experimental results for the external axial force (magenta) and the force model computed using $C_1 = 19$, $C_2 = 0.9$, and $C_3$ = -0.00475 kPa (solid black line) and the optimized Yeoh constants (dotted black line).

and 21.6% increase on $\Delta p$ and $f_{ex}$ respectively. (3) On the other hand, $f_{ex}$ is mostly impacted by $C_3$. A 30% increase in $C_3$ leads to a 24% increase in both the pressure and the axial force model. (4) Both models are equally and lightly impacted by $C_2$. A 30% increase in $C_2$ leads to a 5% increase in the force and pressure model.

### C. Experimental results

Using the set-up in Fig. 5, the thick cylindrical actuator is pressurized, initially without an external axial force, and the resulting pressure is plotted versus the deformations $\lambda_{ex}$ and $\lambda_z$ in Fig. 8. As seen in Fig. 8(a)-(b), using the reference Yeoh model chosen in Section IV ($C_{1r}$ = 15.8, $C_{2r}$ = $-0.48$, and $C_{3r}$ = 0.113 kPa), the pressure model diverges from the experimental results starting at the point ($\lambda_{ex}$ = 2.1, $\lambda_z$ = 1.35). Beyond this state of deformation, the model overestimates the required pressure. For the highest recorded deformation, the pressure calculated with the model is 8 times greater than the experimentally measured pressure. For this reason, the Yeoh model close to the initially chosen one is now considered (red curve in Fig. 4 with $C_1$ = 19, $C_2$ = 0.9, and $C_3$ = -0.00475 kPa). The new computed pressure values with the new Yeoh constants are shown in Fig. 8(c)-(f) (solid blue and solid black curves in Fig. 8(c)-(d) and solid black curves in Fig. 8(e)-(f)). Fig. 8(c)-(d) shows that the new pressure model computed in the absence of an external axial force (solid blue curve) converges towards the experimental results. The curves from the pressure model and the experiments exhibit a similar pattern, albeit with an average deviation of 13.3%. Another experiment is conducted where the cylindrical actuator is simultaneously pressurized and subjected to an external axial load. The results of the pressure and force models are reported in Fig. 8(c)-(f). The pressure and force models (solid black curves in Fig. 8(c)-(f)) grossly overestimate the experimental values (magenta curves in Fig. 8(c)-(f)). Both models yield values at least 2 times the experimental ones with errors over 100% along the range of deformation of the actuator. This significant error suggests that the new chosen Yeoh model might not be the most suitable to describe the material composing the actuator. Therefore, an optimized Yeoh model is computed using a basic optimization function (lsqnonlin in Matlab).

The function takes as input the pressure recorded when an axial force is applied, the corresponding deformations, and the computed model. The optimized Yeoh constants are: $C_1$ = 14.503, $C_2$ = -0.235, and $C_3$ = 0.003 kPa. Obviously, the pressure model computed using the optimized Yeoh constants (dotted black curves in Fig. 8(c)-(d)) gives values very similar to the experimental results (average error of 9%). However, the force model (which is not used in the optimization algorithm) calculated with the optimized Yeoh constants (dotted black curves in Fig. 8(d)-(f)) approaches the experimental results more than the previous one (solid black curve in Fig. 8(d)-(f)) with an average error of 23.6%. In what have preceded, we assumed that the mismatch between the Ecoflex™ 0050 used in the experiments and the material models provided in the literature reviews is the main reason for the significant errors that the pressure and force models. To verify this assumption, we carried out in [15] a preliminary comparative study on the behavior of four geometrically-identical cylindrical actuators fabricated from two different boxes of Ecoflex™ 0050, each of which has been subjected to different storing conditions. All actuators were pressurized and the plots of $\Delta p$ versus $\lambda_{ex}$ and $\lambda_z$ are given. Although the four curves had a similar shape, there was a constant shift between them. For example, the pressure required for actuator 1 is almost always 5 kPa more than that of actuator 2 to reach the same deformation. This result demonstrates the impact of the state of the material used on the experimental results. The comparative study done in [15], the inconsistent and diverse material models found in literature reviews, and their impact on the pressure and axial force models suggest that the material used for the fabrication of the actuators should be characterized beforehand for an informative experimental evaluation.

## V. Conclusion

In this paper, the pressure and axial force models of a thick cylindrical pneumatic actuator are presented along with their detailed proofs. The analytical solutions for these models are derived using the Yeoh strain energy density function. Moreover, an accuracy assessment is done using FEA revealing that the pressure model is accurate up to 7.3% in the absence of an axial force. However, in the presence of an axial force, both the pressure and axial force models tend to underestimate the computed values with FEA for small deformations. For higher levels of deformations, a 6.4% and 10.6% errors are obtained for the pressure and axial force models, respectively. In addition, a sensitivity analysis proves that both models are highly sensitive to the constants of the Yeoh material model. The pressure model is also affected by the radial deformation while the axial force model is sensitive to the axial deformation. Finally, an experimental evaluation demonstrates the importance of the accurate characterization of the material on the experimental and the analytical results.

## References


[1] E. Navas, R. Fernández, D. Sepúlveda, M. Armada, and P. Gonzalez-de Santos, "Soft grippers for automatic crop harvesting: A review," *Sensors*, vol. 21, no. 8, Apr. 2021.

[2] S. Aracri, F. Giorgio-Serchi, G. Suaria, M. E. Sayed, M. P. Nemitz, S. Mahon, and A. A. Stokes, "Soft robots for ocean exploration and offshore operations: A perspective," *Soft Robotics*, vol. 8, no. 6, pp. 625–639, Dec. 2021.

[3] L. Paternò and L. Lorenzon, "Soft robotics in wearable and implantable medical applications: Translational challenges and future outlooks," *Frontiers in Robotics and AI*, vol. 10, Feb. 2023.

[4] D. Haughton and R. W. Ogden, "Bifurcation of inflated circular cylinders of elastic material under axial loading—II. Exact theory for thick-walled tubes," *Journal of the Mechanics and Physics of Solids*, vol. 27, no. 5-6, pp. 489–512, Dec. 1979.

[5] D. M. Taghizadeh, A. Bagheri, and H. Darijani, "On the hyperelastic pressurized thick-walled spherical shells and cylindrical tubes using the analytical closed-form solutions," *International Journal of Applied Mechanics*, vol. 07, no. 02, Apr. 2015.

[6] G. A. Holzapfel, "Hyperelastic materials," in *Nonlinear solid mechanics: a continuum approach for engineering*. Chichester ; New York: Wiley, 2000, ch. 6, p. 243.

[7] A. Pagoli, F. Chapelle, J.-A. Corrales-Ramon, Y. Mezouar, and Y. Lapusta, "Review of soft fluidic actuators: classification and materials modeling analysis," *Smart Materials and Structures*, vol. 31, no. 1, Jan. 2022.

[8] L. Marechal, P. Balland, L. Lindenroth, F. Petrou, C. Kontovounisios, and F. Bello, "Toward a common framework and database of materials for soft robotics," *Soft Robotics*, vol. 8, no. 3, pp. 284–297, Jun. 2021.

[9] M. S. Xavier, C. D. Tawk, A. Zolfagharian, J. Pinskier, D. Howard, T. Young, J. Lai, S. M. Harrison, Y. K. Yong, M. Bodaghi, and A. J. Fleming, "Soft pneumatic actuators: A review of design, fabrication, modeling, sensing, control and applications," *IEEE Access*, vol. 10, pp. 59 442–59 485, Sep. 2022.

[10] X. Yao, Z. Wang, L. Ma, Z. Miao, M. Su, X. Han, and J. Yang, "Temperature dependence of rubber hyper-elasticity based on different constitutive models and their prediction ability," *Polymers*, vol. 14, no. 17, Aug. 2022.

[11] A. Valiollahi, M. Shojaeifard, and M. Baghani, "Closed form solutions for large deformation of cylinders under combined extension-torsion," *International Journal of Mechanical Sciences*, vol. 157-158, pp. 336–347, Jul. 2019.

[12] S. Mehta, G. Raju, S. Kumar, and P. Saxena, "Instabilities in a compressible hyperelastic cylindrical channel due to internal pressure and external constraints," *International Journal of Non-Linear Mechanics*, vol. 144, p. 104031, Sep. 2022.

[13] X. Yu and Y. Fu, "A one-dimensional model for axisymmetric deformations of an inflated hyperelastic tube of finite wall thickness," *Journal of the Mechanics and Physics of Solids*, vol. 175, p. 105276, Jun. 2023.

[14] O. H. Yeoh, "Some forms of the strain energy function for rubber," *Rubber Chemistry and technology*, vol. 66, pp. 745–771, Nov. 1993.

[15] Z. Awada, H. E. Jjouaui, Y. Haddab, and M. Gouttefarde, "Supplementary materials - modeling of a thick cylindrical pneumatic leg for a soft parallel robot." [Online]. Available: https://hal.science/hal-04266898

[16] D. Sarkar, S. Chakraborty, A. Arora, and S. Sen, "A reinforced soft bending-type actuator with improved performance and force sensing: Design, analysis and experiments," in *Advances in Robotics - 5th International Conference of The Robotics Society*. Kanpur India: ACM, Jun. 2021, pp. 1–6.

[17] G. Runge, M. Wiese, L. Gunther, and A. Raatz, "A framework for the kinematic modeling of soft material robots combining finite element analysis and piecewise constant curvature kinematics," in *2017 3rd International Conference on Control, Automation and Robotics (ICCAR)*. Nagoya, Japan: IEEE, Apr. 2017, pp. 7–14.

[18] L. Chen, C. Yang, H. Wang, D. T. Branson, J. S. Dai, and R. Kang, "Design and modeling of a soft robotic surface with hyperelastic material," *Mechanism and Machine Theory*, vol. 130, pp. 109–122, Dec. 2018.

[19] Z. Xue, Q. Wu, and F. Gao, "Design and modeling of omni-directional bending pneumatic flexible arm," in *2018 3rd International Conference on Advanced Robotics and Mechatronics (ICARM)*, Singapore, Singapore, 2018, pp. 835–839.

[20] M. S. Xavier, A. J. Fleming, and Y. K. Yong, "Finite element modeling of soft fluidic actuators: Overview and recent developments," *Advanced Intelligent Systems*, vol. 3, no. 2, Feb. 2021.